International Journal of Microwave and Wireless Technologies

cambridge.org/mrf

Mutual coupling reduction of two-port dielectric resonator MIMO antenna using defected ground structure

Gouri Shankar Sharma and Anshul Gupta

Department of Electronics & Communication Engineering, NIT, Raipur, India

Research Paper

Cite this article: Sharma GS, Gupta A (2024) Mutual coupling reduction of two-port dielectric resonator MIMO antenna using defected ground structure. *International Journal of Microwave and Wireless Technologies*, 1–15. https://doi.org/10.1017/S1759078724000862

Received: 11 August 2023
Revised: 14 August 2024
Accepted: 18 August 2024

Keywords:
Dielectric resonator; diversity; defective ground structure; mutual coupling; MIMO; WLAN; WiMAX

Corresponding author: Anshul Gupta; Email: agupta.etc@nitrr.ac.in

Abstract

This article focuses on reducing mutual coupling between the ports of dielectric resonator antenna (DRA) using defected ground structures (DGSs). The antenna has the dimension of 50 mm × 50 mm × 8.5 mm. The resonating element in the proposed two-port radiator consists of a cylindrical structure of alumina ceramic ($\varepsilon_r = 9.8$). The rectangular-shaped aperture is utilized to excite both of the resonating elements. The resonating ceramic elements acting as radiators are offset-fed to enhance the antenna's coupling. Combining interdigital-shaped and semicircular arc-shaped DGSs improves isolation between two resonating elements, embodying the structural novelty. The measured operating frequency range of Port-1 and Port-2 is 5.19–6.7 and 5.15–6.68 GHz, resonating at 5.58 and 5.56 GHz, respectively. The measured mutual coupling between the two ports is −35.5 dB. The measured gain for Port-1 is depicted to be 5.5 dB. The presented multiple-input–multiple-output (MIMO) radiator in this article is an appropriate candidate for WLAN (5.25–5.35, 5.47–5.725, 5.725–5.85, 5.850–5.925 GHz) and WiMAX (5.5 GHz) applications. All the simulated and experimentally observed MIMO parameters of the radiator are discovered to be within optimal bounds.

Introduction

Multiple-input–multiple-output (MIMO) antenna technology is a vital element in modern wireless communication systems. It enables the concurrent transmission and reception of multiple data streams, leading to increased system capacity, improved spectrum efficiency, and enhanced data throughput. MIMO systems harness the spatial diversity of the wireless channel by utilizing multiple antennas, unlike traditional single-input, single-output systems that rely on a single antenna at each end [1–4]. The utilization of dielectric resonator (DR)-based MIMO antennas offers negligible conduction losses, wider bandwidth, and high radiation efficiency compared to metallic MIMO antennas. Designing MIMO antennas requires careful consideration of strategies to reduce mutual coupling or improve isolation. Due to mutual coupling, which takes place when antennas are placed close to one another, and one transmits a signal that interferes with another antenna's reception of a signal, MIMO systems use several antennas. Because of this, the system's performance may suffer, leading to higher bit error rates or lower data rates [5].

A vast number of articles on port-to-port mutual coupling reduction (isolation improvement) are available in the literature [6–29], which includes utilization of electromagnetic bandgap structure, neutralization lines, parasitic elements, metamaterial, metasurfaces, frequency selective surface, antenna spacing between radiating elements, defected ground structure (DGS), generation of orthogonal modes, metal strip printed on dielectric resonator (DR), and positioning of split-ring resonator (SRR) printed substrate between radiators. The isolation improvement techniques reported in Refs [6–19] have complex design procedures, while the method reported in Ref. [20] is the easiest but leads to more oversized/bulky antenna designs. The technique illustrated in Refs [21, 22] has a more effortless fabrication procedure due to its planar structure. The isolation enhancement technique used for MIMO antenna design, as reported in Ref. [23] by Jamal et al. in 2014, is the generation of orthogonal modes. It involved a dual-port rectangular DRA fed orthogonally with the aid of two symmetrical feed lines for isolation enhancement. It provided an isolation of −18 dB at a resonant frequency of 1.8 GHz. However, this antenna suffered from low bandwidth, low isolation, and fabrication complexity, highlighting the need for advanced techniques and solutions in MIMO antenna design. Das et al. examined a cylindrical DRA-based MIMO antenna in 2017. The MIMO radiator achieved isolation of −32 dB through the generation of orthogonal modes in the cylindrical DRA,

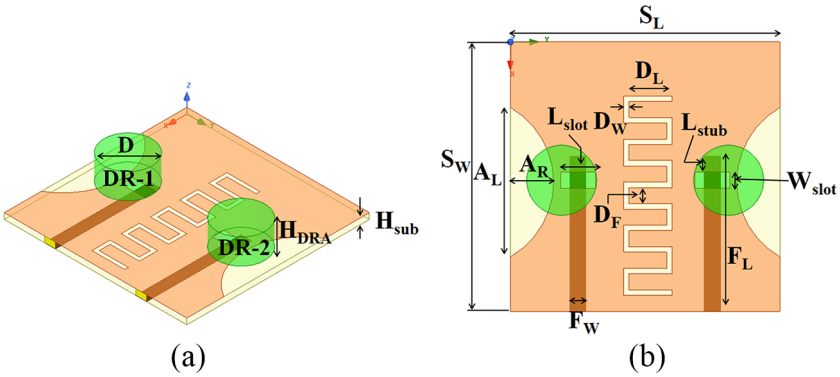

Figure 1. Structure of the proposed two-port radiator: (a) 3D view, (b) Top view.

employing dual-feeding strategies: slot coupling (Port-1) and coplanar waveguide (Port-2) approaches. However, the fractional bandwidth was limited to 11.5% (4.9–5.5 GHz) [24]. An orthogonal fed MIMO DRA with two ports was presented in Ref. [25] in 2017 and was excited by utilizing the dual feeding method. The feeding elements were positioned to generate an orthogonal mode when interacting with the DR. In this radiator, by producing two orthogonal modes, i.e. $HE^{y}_{11\delta}$ and $HE^{x}_{11\delta}$, isolation better than −25 dB was observed between the two ports. The fractional bandwidth for Port-1 was found to be 17.8% (3.1–3.68 GHz), while Port-2 was discovered to be 18.4% (3.1–3.7 GHz).

Zhang et al. presented a two-port MIMO radiator in 2019 [26]. In this rectangular DRA-based MIMO antenna, to increase the isolation between two antenna elements, each DR has a metallic tape fixed on the upper surface that shifts the coupling field's strongest portion away from the exciting slot; as a result, the isolation of −24 dB was observed in the operating frequency band 27.5–28.35 GHz. The positioning of metallic taps requires high precision, which leads to fabrication complexity. Manzoor et al. proposed a two-port MIMO DRA in a study conducted in 2022, with an operating frequency range of 4.73–5.1 GHz [27]. This MIMO structure utilized closed metallic loops to minimize mutual coupling between radiators. For this intent, the edges of DRA were encircled with a loop in the region of the strong magnetic field. The measured isolation was found to be −28 dB at the resonance frequency. However, this antenna suffered a lower fractional bandwidth of only 3%. A quad-port MIMO radiator working in the frequency range 4.48–4.60 and 4.98–5.04 GHz was proposed in 2022 by Upadhyaya et al. [28]. In this radiator, an orthogonal arrangement of antenna elements was utilized to reduce mutual coupling, resulting in an isolation of −22.5 dB at 4.5 GHz and −24.98 dB at 5 GHz, respectively. This antenna suffered poor band coverage in both bands. In the other study in 2022, a two-port cylindrical MIMO DRA was proposed by Mishra et al., which utilized a wall equipped with a SRR between antenna elements for isolation enhancement [29]. The radiator operated in the frequency band 7.40–7.80 GHz and provided an isolation of −30 dB at resonating frequency. This antenna again agonized fabrication complexity.

In the proposed two-port radiator, coupling coefficient, bandwidth, and isolation improvement have been provided by simultaneously combining arc-shaped DGS and interdigital-shaped

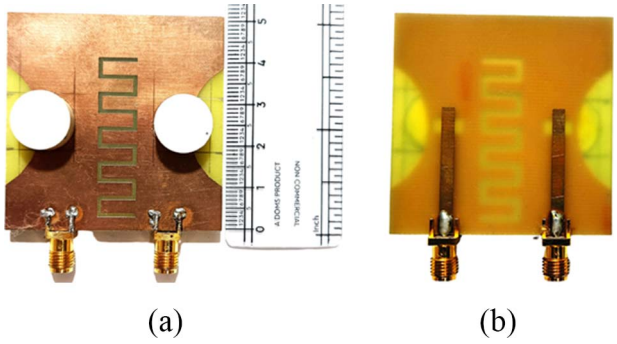

Figure 2. Fabricated antenna: (a) Top View, (b) Bottom View.

DGS. The proposed two-port radiator utilizes cylindrical-shaped alumina ceramic as a radiating element. It is offset-fed with a rectangular aperture to enhance the feedline and DRA coupling. The measured operating band for Port-1 and Port-2 of the proposed two-port radiator is found to be 5.19–6.7 and 5.15–6.68 GHz, whereas isolation between the antenna elements is determined to be −35.5 dB at the frequency of resonance. All the other parameters of the proposed MIMO radiator, like gain, radiation pattern, and MIMO metrics like envelope correlation coefficient (ECC), diversity gain (DG), mean effective gain (MEG), total active reflection coefficient (TARC), and Channel Capacity Loss (CCL) have been simulated and verified through measurement and are found to be within optimal limits. The formulation of the proposed antenna, antenna analysis, equivalent circuit of the proposed antenna, experimental results, diversity parameters, and conclusion have been depicted in the respective sections.

Formulation of the proposed antenna

The proposed two-port radiator configuration consists of two ceramic cylindrical dielectric resonators (CDR) made up of alumina ($\varepsilon_r = 9.8$), mounted upon a FR-4 substrate ($\varepsilon_r = 4.4$). The two resonators are energized with a microstrip feed line through a rectangular slot and are offset-fed to enhance the coupling between the alumina ceramic resonator and aperture. The length of the feed line is obtained through optimization. An interdigital-shaped and semicircular arc-shaped DGS

https://doi.org/10.1017/S1759078724000862 Published online by Cambridge University Press

Table 1. Dimensions of proposed two-port MIMO antenna

Parameter	Value (mm)	Parameter	Value (mm)
$S_L = S_w$	50	D	6.9
H_{sub}	1.6	H_{DRA}	6.9
F_L	28.8	D_w	1
F_w	3	L_{stub}	2.9
L_{slot}	6.5	A_L	27.7
W_{slot}	3.1	A_R	8
D_L	8		

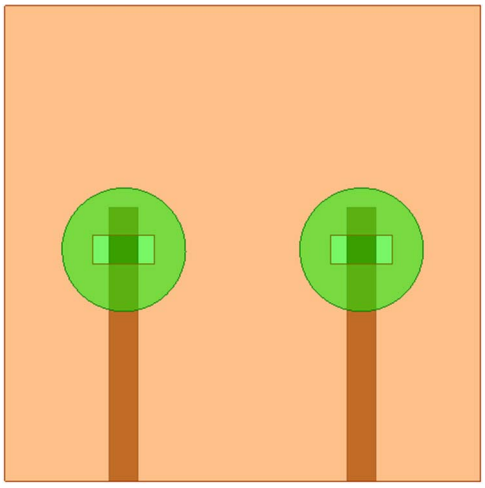

Figure 3. Antenna-1 (stage-1).

enhances the isolation between two radiators and controls the operating band. Figure 1 represents the proposed structure of a two-port DRA. Figure 2 represents the fabricated two-port MIMO radiator. The antenna dimensions have been depicted in Table 1.

Antenna analysis

The proposed two-port radiator has been simulated and examined using electromagnetic simulation software called HFSS. Stage-by-stage analysis of the two-port radiator is illustrated in Figs. 3–11. Initially, DRs were excited through the center-feed with the aid of a rectangular aperture, which is named Antenna-1, as displayed in Fig. 3. The frequency band was obtained 5.57–6.15 GHz having a reflection coefficient −17 dB for Port-1 at the resonant frequency of 5.84 GHz. This antenna suffered poor band coverage, poor reflection coefficient, and poor isolation. In the next step, the DRs were excited through the offset feeding technique as shown in Fig. 4, and named Antenna-2. The reflection coefficient and isolation were improved to −23.2 and −22.8 dB, respectively, covering the 5.65–6.28 GHz frequency range. The improvement in the reflection coefficient was observed due to improved impedance matching between the radiators and the feedline [30]. The improvement in isolation was observed due to a reduction in the surface currents flowing in the adjacent radiators [31]. However, at this

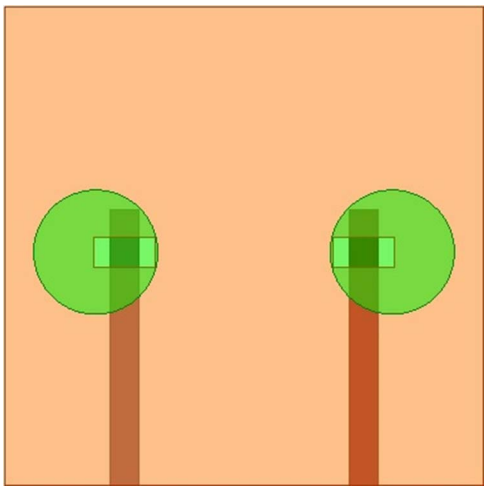

Figure 4. Antenna-2 (stage-2).

stage, the antenna also does not cover the entire upper WLAN band.

Next, a semicircular arc-shaped DGS was applied beneath the two DRs named Antenna-3 and displayed in Fig. 5(a) to achieve the desired operating band. The dimensions of the DGS were precisely estimated through a rigorous optimization process using the powerful HFSS software. This antenna improved WLAN band coverage and occupied the frequency band 5.07–6.10 GHz (desired operating band). The reflection coefficient and isolation were also enhanced to − 33 and − 31 dB, respectively, at the resonating frequency of 5.48 GHz. A parametric analysis of its different radii (A_R = 2,4,6,8 mm) was conducted to determine the effects on operating frequency and isolation. The scattering parameter (S-parameter) and surface current distribution of the ground plane (keeping Port-1 excited and Port-2 terminated) were plotted as depicted in Fig. 5(b) and Fig. 5(c). From Fig. 5(b), it can be observed that at A_R = 8 mm, the antenna achieves the desired operating band. In contrast, from Fig. 5(c), it can be analyzed that the concentration of surface currents is more toward the periphery of arc-shaped DGS (for A_R = 8 mm) located beneath DR-1, in comparison to the arc-shaped DGS beneath DR-2 leading to improved isolation. The E-field distribution of the ground plane for A_R = 8 mm is also plotted for more confirmation, as presented in Fig. 6. In this case, high electric field concentrations are observed at the periphery of the semicircular arc-shaped DGS. The concentration of fields and surface currents at the periphery of arc-shaped DGS relies on the area covered on the ground plane. The wider the area of arc-shaped DGS, the more concentration of fields and surface currents are at its periphery, which means improved isolation. A similar condition was observed in arc-shaped DGS (located on the right side) beneath DR-2 when Port-2 is excited, and Port-1 is terminated. The area covered by the semicircular arc-shaped DGS is also responsible for controlling the operating frequency span of the proclaimed antenna. The desired operating band can be achieved by varying the area of the DGS [32]. The slotted area of the DGS signifies effective inductance and is inversely proportional to effective capacitance. Enlarging the DGS area results in increased effective inductance and a lower operating frequency. Conversely, reducing the DGS area lowers

https://doi.org/10.1017/S1759078724000862 Published online by Cambridge University Press

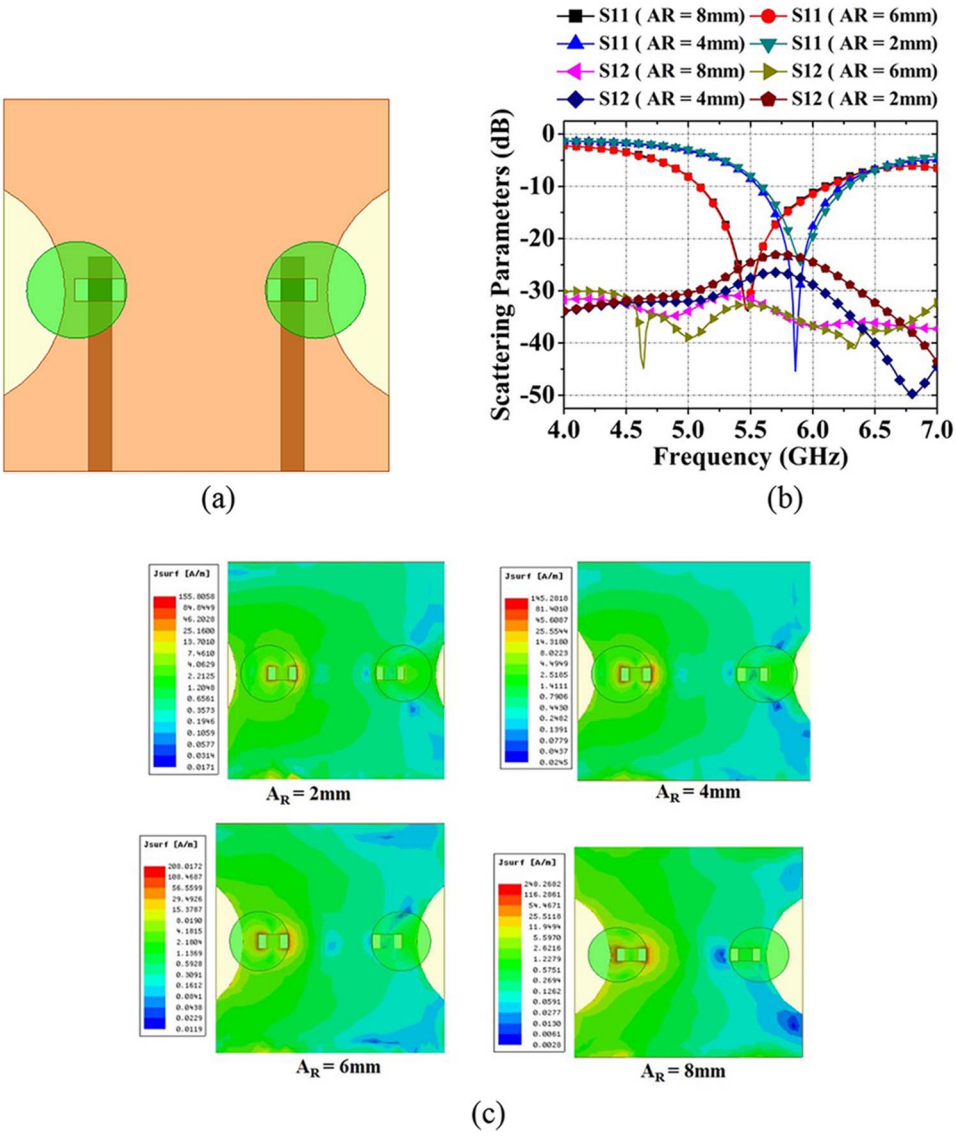

Figure 5. Parametric analysis for various radii (A_R) of arc-shaped DGS of Antenna-3(stage-3): (a) Structure, (b) Scattering parameters, and (c) Surface current distribution.

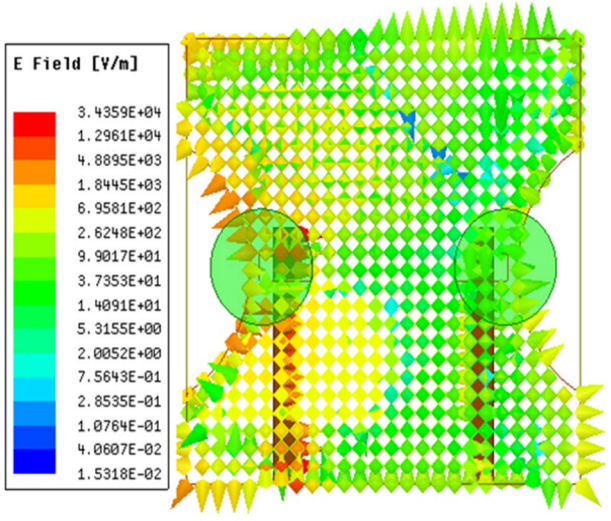

Figure 6. Simulated E-field distribution of ground plane at $A_R = 8$ mm.

effective capacitance, leading to a higher resonant frequency [33]. In the next stage in Antenna-4, the interdigital-shaped DGS was applied between the two DRs to improve isolation, as depicted in Fig. 7(a). The operation of interdigital-shaped DGS is validated with the help of its equivalent circuit, as shown in Fig. 7(b) [34]. The equivalent circuit of the proposed structure, illustrated in Fig. 7(b), is a combination of the interdigital capacitance equivalent circuit and the equivalent circuit of the DGS (represented by inductance L_p). The series circuit CL_s represents an equivalent circuit of the interdigital capacitance. A parametric analysis is conducted on various numbers ($N = 5, 7, 10$) of metal fingers, finger length (D_L), and spacing between fingers (D_F)by keeping the radius ($A_R = 8$ mm) of the semicircular arc-shaped DGS constant. It is found that for $N = 5$, improvements in isolation compared to Antenna-3 are not observed at resonant frequency. The Antenna-4 achieved isolation of −30.2 dB at resonant frequency. On increasing the number of metal fingers ($N = 7, 10$), an improvement in isolation is observed due to low surface currents amid the two radiators of the proposed antenna. Maximum

https://doi.org/10.1017/S1759078724000862 Published online by Cambridge University Press

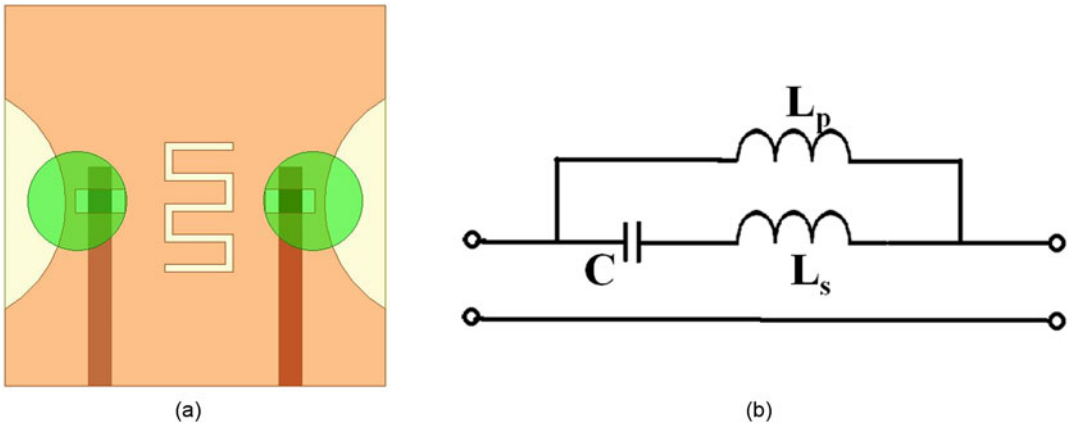

Figure 7. Antenna-4 (stage-4): (a) Structure, (b) Equivalent circuit of interdigital-shaped DGS.

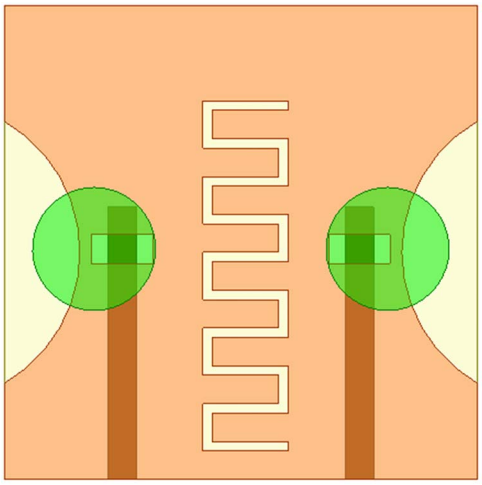

Figure 8. Proposed two-port antenna, Antenna-5 (stage-5.

isolation of −38 dB is obtained for $N = 10$ in the proposed antenna (Antenna-5) depicted in Fig. 8, working within the frequency spectrum of 5.07–6.08 GHz. For validation, S-parameters and surface current distribution graphs are depicted in Fig. 9(a) and (b), respectively.

Further, by varying finger length, it is found that the resonant frequency and isolation are also altered. The shift in the resonant frequency is observed due to variation of capacitance "C", and variation in isolation is due to increment/decrement of the path length of surface current flowing between two radiators. An increased path length provides improved isolation between two radiators. S-parameters and surface current distribution graphs are rendered in Fig. 10(a) and (b) to further validate the effect of finger length on different finger lengths. The graphs confirm that for $D_L = 8$ mm, the desired result (isolation of −38 dB) is obtained.

The final analysis is done on the variation of spacing between fingers (D_F). Variation in the spacing between fingers also alters the surface current path length. For $D_F = 3$ mm (value in proposed antenna −5), the desired isolation of −38 dB is obtained. However, there is no influence on the operating frequency of the proposed antenna by varying spacing between the fingers. For validation, the S-parameters plot and surface current distribution graphs are rendered in Fig. 11(a) and (b). Hence, from the analysis elaborated above, it is confirmed that the combination of semicircular arc-shaped DGS and interdigital-shaped DGS provides the desired operating band for the upper band of WLAN and good isolation.

The graphical representation in Fig. 12 illustrates the reflection coefficient ($|S_{11}|$), isolation ($|S_{12}|$) for Port-1 of all antennas (Antenna-1 to Antenna-5) and their impedances. The simulated S-parameters and impedance of the designed radiator have been presented in Fig. 13(a) and Fig. 13(b) respectively. The reflection coefficients of Port-1 and Port-2 are determined to be −37.1 and − 34.1 dB, covering the frequency band of 5.07–6.08 and 5.06–6.07 GHz, respectively. The impedance of the antenna was found to be close to 50 Ω. The E-field distribution of Port-1 and Port-2 of the proposed two-port radiator at resonant frequencies 5.46 and 5.43 GHz is demonstrated in Fig. 14(a) and (b) in XY- and YZ- plane, respectively. It can be observed that $HE_{11\delta}$ mode is excited for Port-1 and Port-2 in the proposed two-port radiator. The resonance frequency of the CDR antenna for $HE_{11\delta}$ mode is computed using the equations (1–3) [35, 36].

$$f_r = \frac{6.321\nu}{2\pi X\sqrt{\varepsilon_{r,eff}+2}}\left[0.27 + 0.36\left(\frac{X}{2H_E}\right) + 0.02\left(\frac{X}{2H_E}\right)^2\right] \quad (1)$$

In the case of the CDR antenna, the speed of light is depicted by ν, the effective relative permittivity is represented by $\varepsilon_{r,\,eff}$, the radius is demonstrated by "X", ($X = D/2$), and the equivalent height H_E of the proposed two-port radiator is assessed as per Ref. [35]:

$$\varepsilon_{r,\,eff} = \frac{H_E}{\frac{H_{DRA}}{\varepsilon_{alumina}} + \frac{H_{sub}}{\varepsilon_{sub}}} \quad (2)$$

and

$$H_{E=}H_{DRA} + H_{sub} \quad (3)$$

The computed resonant frequency (theoretical) is determined to be 5.8 GHz while the simulated is observed to be 5.84 GHz (Antenna-1). The computed and simulated frequencies of resonance are observed to be in close contiguity.

https://doi.org/10.1017/S1759078724000862 Published online by Cambridge University Press

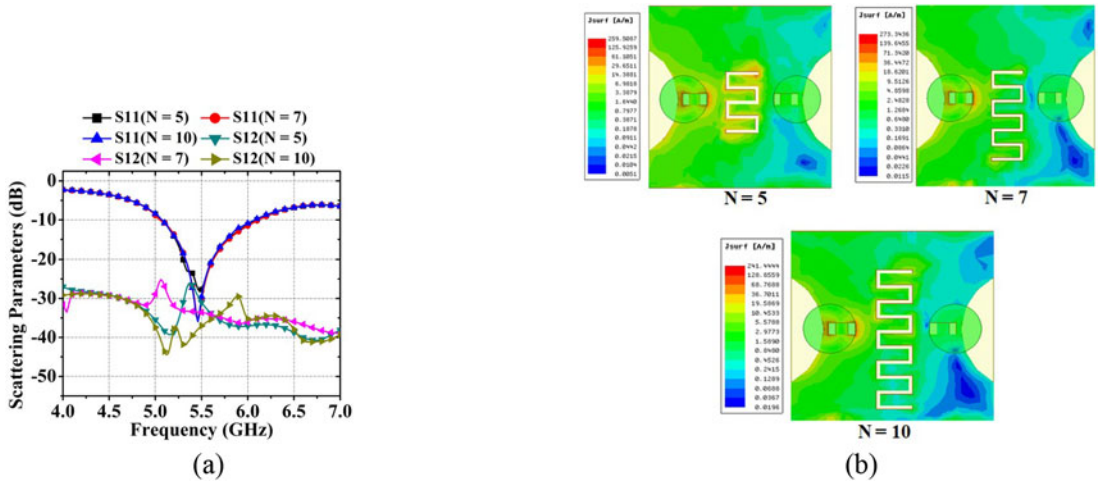

Figure 9. Simulation analysis for various numbers (*N*) of metal fingers: (a) Scattering parameters, (b) Surface current distribution.

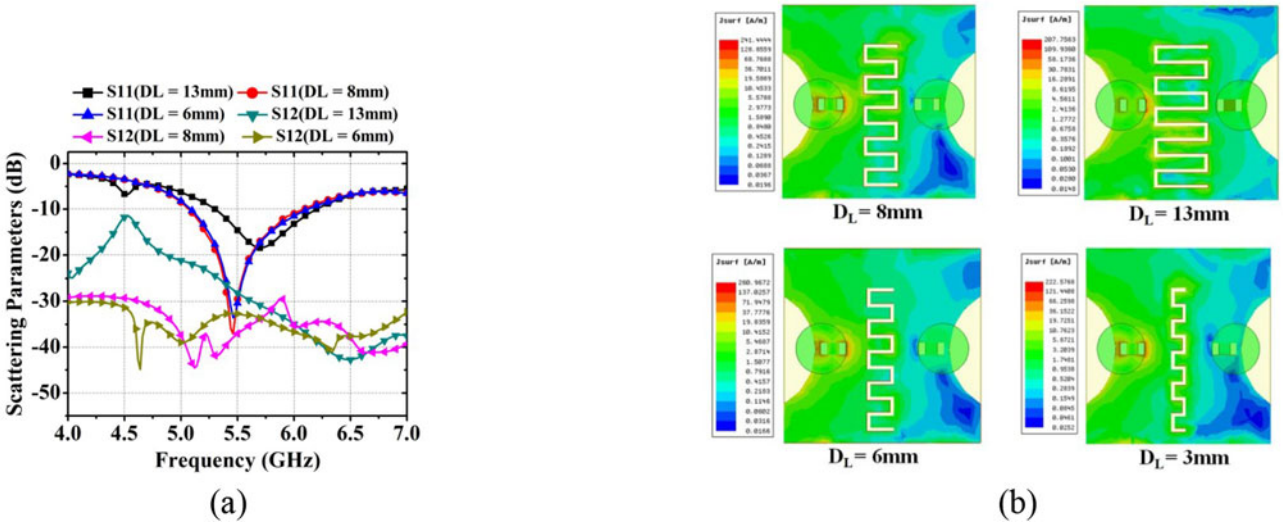

Figure 10. Simulation analysis for various finger lengths (D_L): (a) Scattering parameters, (b) Surface current distribution.

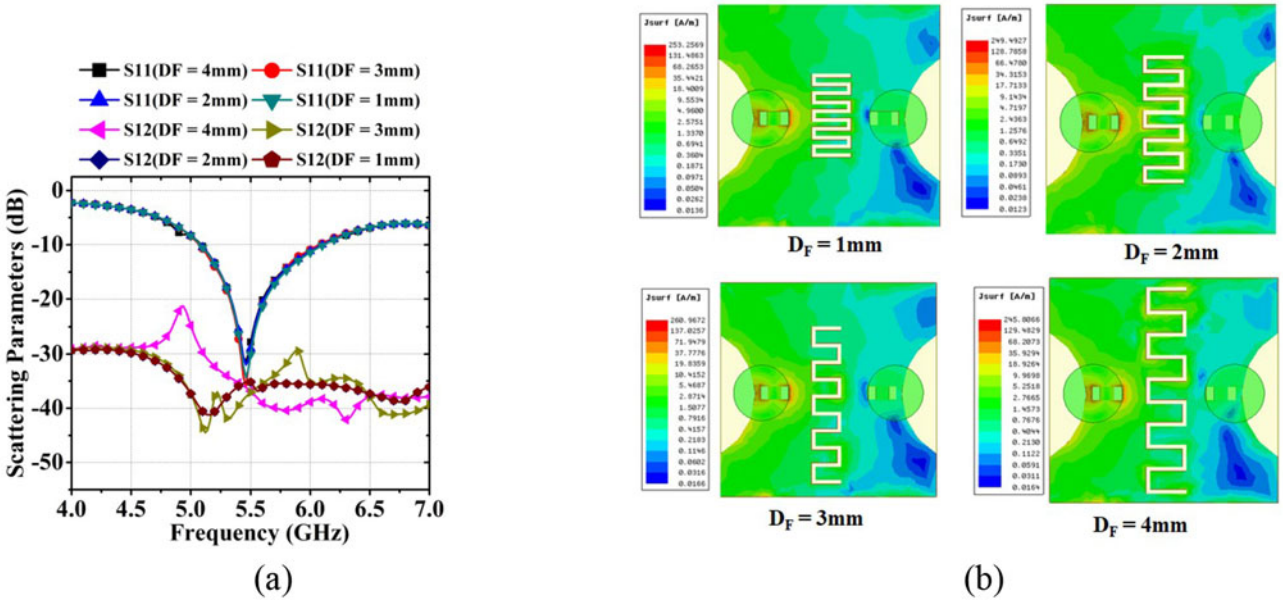

Figure 11. Simulation analysis for various finger spacing (D_F): (a) Scattering parameters, (b) Surface current distribution.

https://doi.org/10.1017/S1759078724000862 Published online by Cambridge University Press

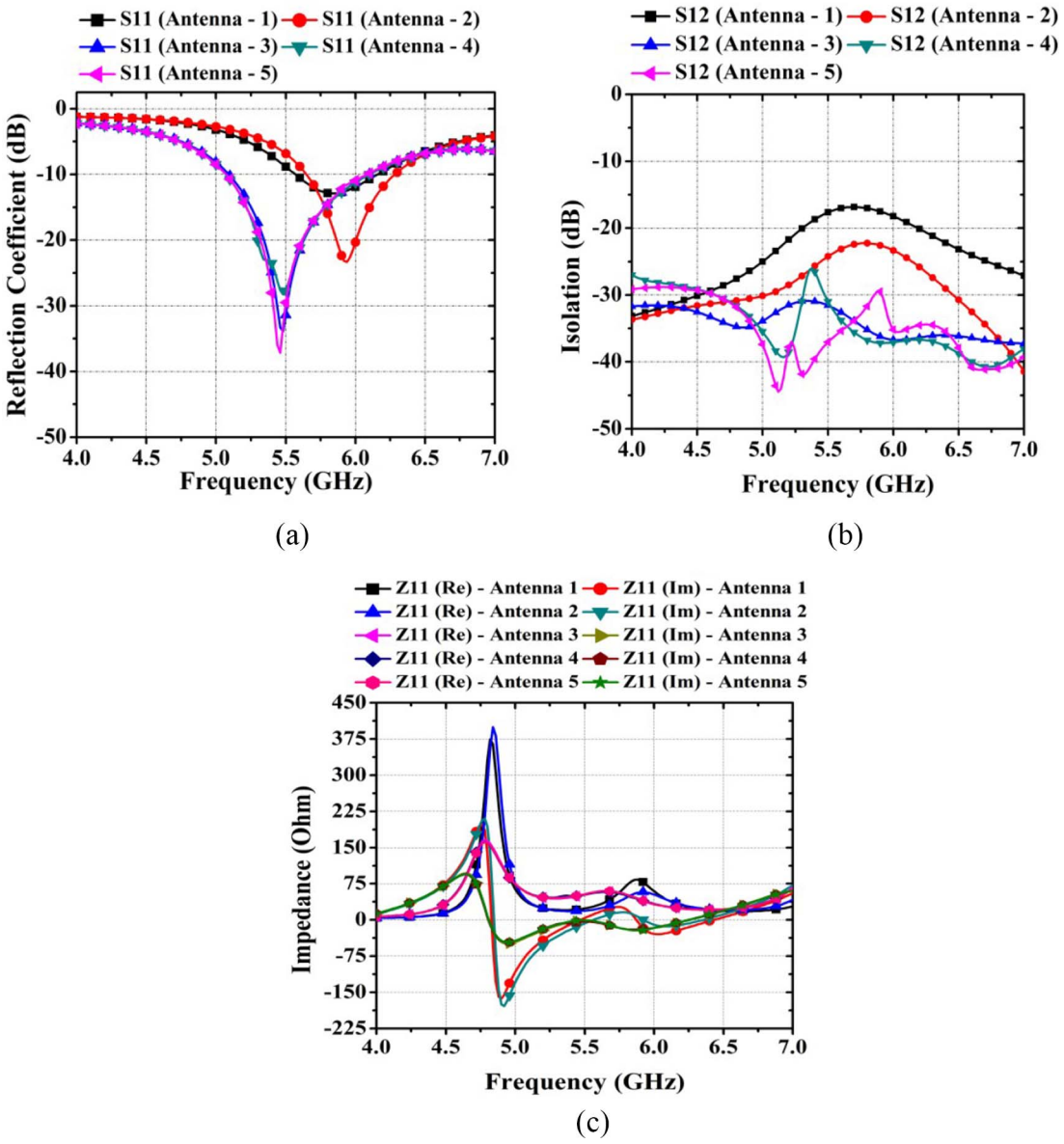

Figure 12. Simulation analysis of Antenna-1 to Antenna-5: (a) Reflection coefficient, (b) Isolation, and (c) Impedance.

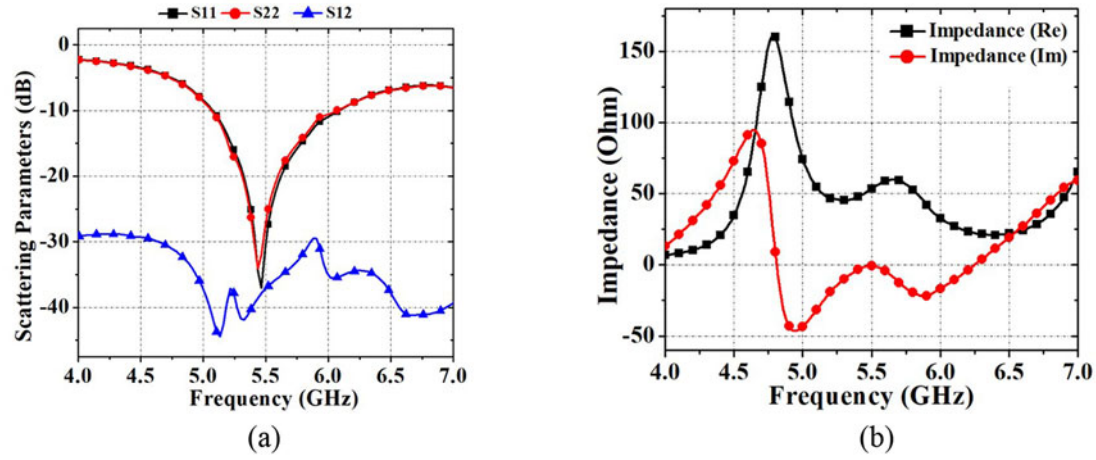

Figure 13. Simulated antenna parameters of the proposed two-port radiator (Antenna-5): (a) Scattering parameter and (b) Impedance.

https://doi.org/10.1017/S1759078724000862 Published online by Cambridge University Press

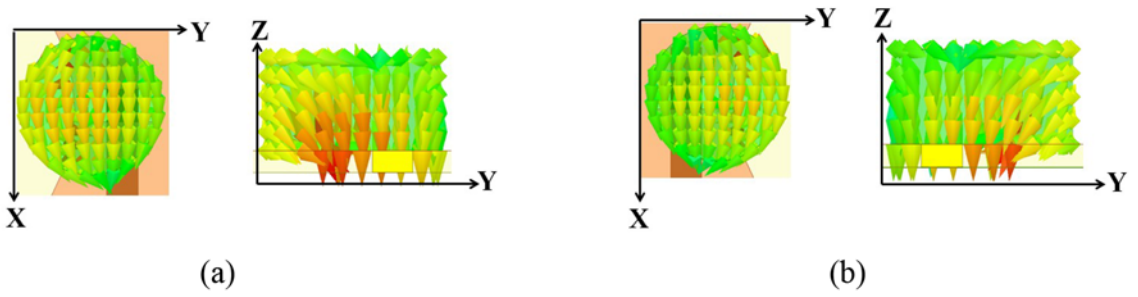

Figure 14. E-field distribution of proposed two-port radiator (a) Port-1at 5.46 GHz and (b) Port-2 at 5.43 GHz.

Table 2. Calculated values of equivalent circuit elements

Prameters of equivalent circuit model				
$X_1 = X_4$ =0.8	$X_2 = X_5$ =1.2	$X_3 = X_6$ =0.7	$L_1 = L_7$ =0.5 nH	$L_2 = L_6$ =1.32 nH
$L_4 = L_8$ =0.21 nH	$L_5 = L_9$ = 0.3 nH	L_s =24 nH	L_p =22 nH	C =1 pF
$C_2 = C_5$ =1.2 pF	$C_3 = C_7$ =1 pF	$C_4 = C_8$ =0.3 pF	$R_1 = R_4$ =10 Ω	$R_2 = R_5$ =50 Ω
$L_3 = L_{10}$ =1.59 nH	$C_1 = C_6$ =8.71 pF	$R_3 = R_6$ =50 Ω		

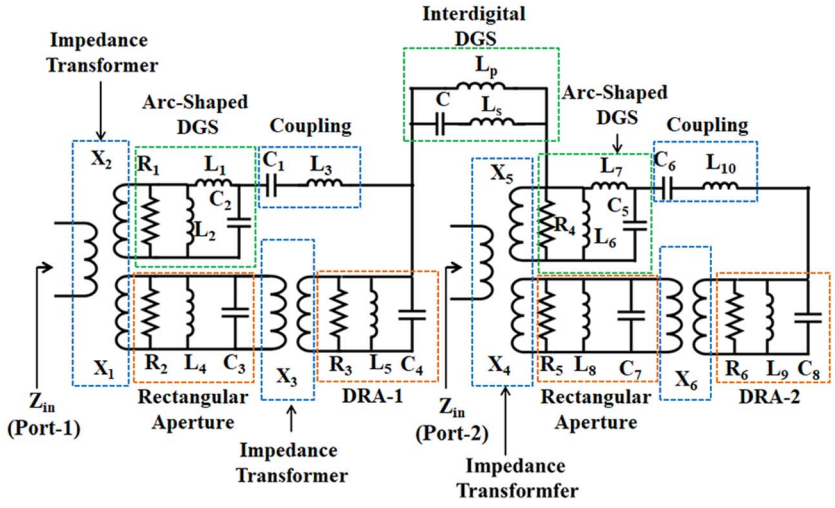

Figure 15. Equivalent circuit model of two-port radiator.

Equivalent circuit of proposed antenna

The equivalent circuit model with calculated RLC parameters (Table 2) is depicted in Fig. 15 to validate the scattering parameter response of the proclaimed two-port antenna. The rectangular aperture and arc-shaped DGS beneath the DR consist of an RLC circuit. The rectangular aperture interfaces with a microstrip transmission line and CDR through an impedance transformer. The coupling between arc-shaped DGS and DR is done via an LC circuit.

Experimental results

The circuit model for interdigital DGS utilized for isolation enhancement is depicted by inductors "Lp" and "Ls" and capacitor "C". The S-parameters extracted from the equivalent circuit have been compared with S parameters obtained through HFSS, and the parameters obtained from the measurement are rendered in the "Experimental results" section. The extracted S-parameters from the equivalent circuit of the antenna are compared with the simulated S-parameters (using HFSS) and experimentally observed S-parameters whose plots are depicted in Fig. 16(a–c). Scattering parameter measurement is performed using Keysight N9917A Fieldfox Vector Network Analyzer (VNA), presented in Fig. 17. Table 3 demonstrates the distinction between the simulated, circuit model, and measured input parameters. Figure 16(a) and (b) and Table 3 reveal that the simulated fractional bandwidth for Port-1 is 18.11% and for Port-2 is 18.14%. The circuit model indicates a bandwidth of 18.16% for Port-1 and 18.52% for Port-2, while the measured bandwidths are 25.40% and 25.87% for Port-1 and Port-2, respectively. The isolation (mutual coupling) obtained through simulation, circuit modelling, and measurement, as rendered in Fig. 16(c), are observed to be −38, −39.27, and −35.5 dB, respectively. The simulated S-parameters and S-parameters extracted from the equivalent circuit mentioned in Fig. 15 are found close to each other with slight variation, possibly due to distinct mathematical techniques utilized by HFSS and circuit modeling software [37]. The

https://doi.org/10.1017/S1759078724000862 Published online by Cambridge University Press

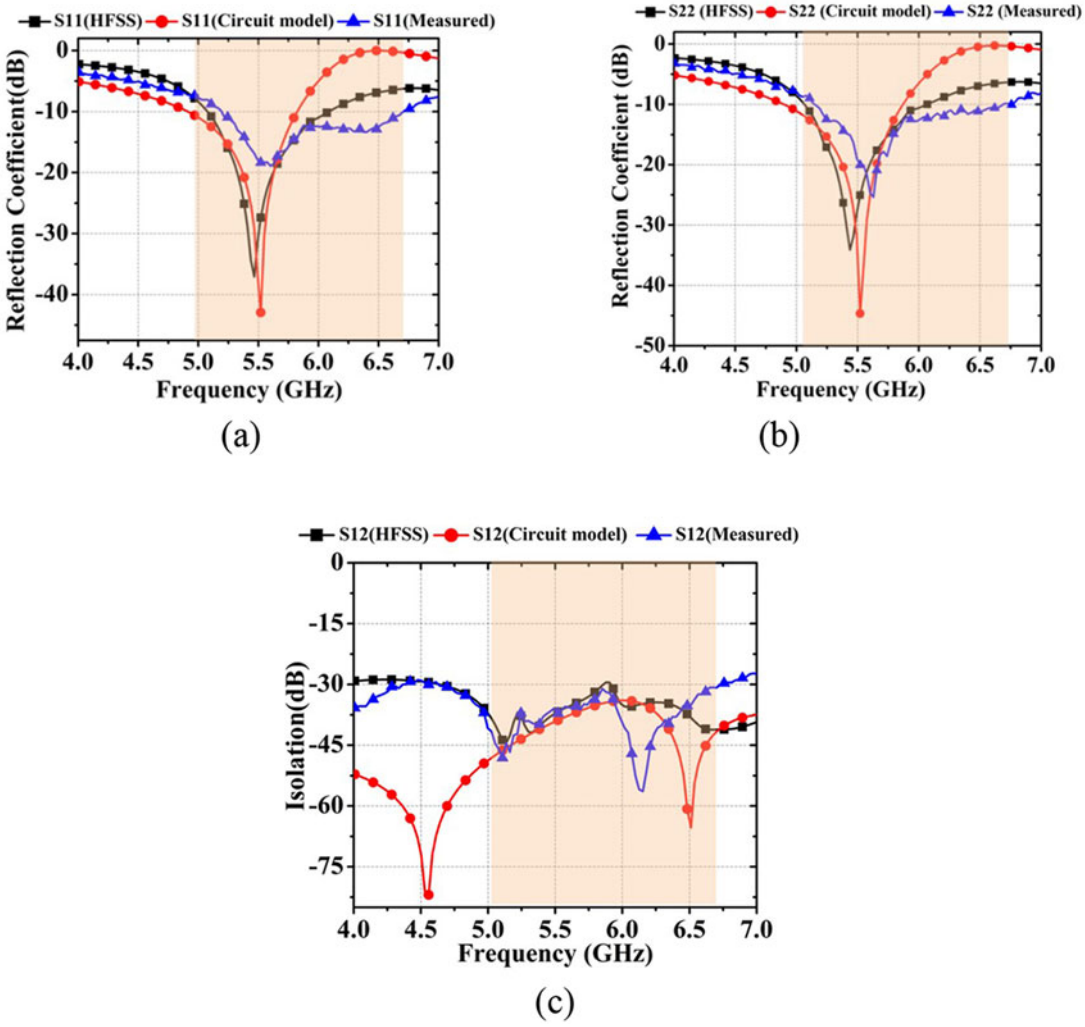

Figure 16. Comparison between simulated (using HFSS), circuit model, and experimental S-parameters of the proposed two-port radiator: (a) S_{11}, (b) S_{22}, and (c) S_{12}.

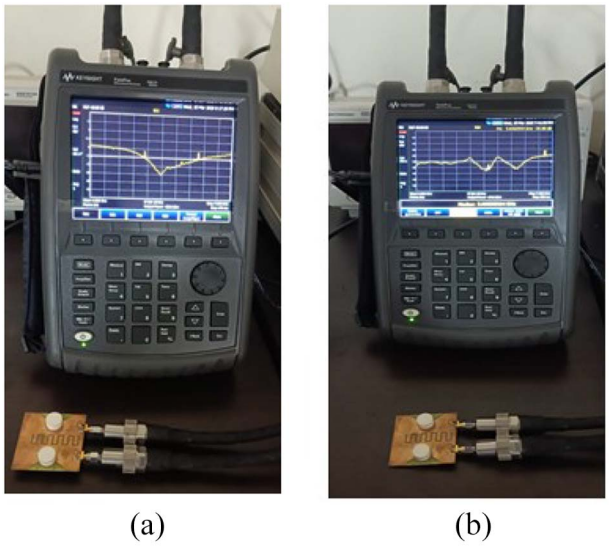

Figure 17. Experimental setup for measurement of S-parameters of the proposed two-port radiator: (a) Reflection coefficient (S_{11}) and (b) Isolation. The radiation efficiency of the proposed two-port radiator (Antenna-5) exceeded 93% for both Port-1 and Port-2, respectively. The gain and radiation pattern measurements were conducted in an automatic anechoic chamber, as illustrated in Figure 20.

distinctness in experimental S-parameters is also noticed, which may be due to the adhesive used to mount DRA on the substrate and other fabrication discrepancies. By applying an adhesive material, a thin dielectric layer is introduced between the substrate and the CDR. This arrangement results in a reduction of the effective permittivity within the proposed structure. Consequently, the quality factor decreases while the bandwidth experiences an improvement, as evidenced by the measured results [38]. Figure 18(a) and (b) depicts the comparison amidst the simulated and experimentally observed far-field radiation patterns regarding the E-plane and H-plane for Port-1 and Port-2, respectively.

It is noticeable that in the broadside direction, i.e. ($\theta = 0$, $\phi = 0$), the antenna shows maximum radiation, and the cross-polarization is found below co-polarization for both the ports below −25 dB, which is required for any low loss MIMO radiator. Close consistency was noticed amidst the simulated and measured radiation patterns for both ports. In Fig. 19, the comparison between the simulated and measured gain plots for Port-1 is depicted, and they were found to be close to each other. The measured gain for Port-1 at resonant frequency was found to be 5.5 dB. The comparison between simulated and measured gain for Port-2 has not been incorporated due to its identical nature to that of Port-1.

https://doi.org/10.1017/S1759078724000862 Published online by Cambridge University Press

Table 3. Comparative analysis between simulated (using HFSS), circuit model, and measured input parameters

	Simulated (HFSS)		Circuit model		Measured	
Parameters	Port-1	Port-2	Port-1	Port-2	Port-1	Port-2
Reflection coefficient (dB)	−37.1	−34.1	−45	−45	−18.64	−24.4
Resonant frequency (GHz)	5.46	5.43	5.5	5.5	5.58	5.6
Isolation (dB)	−38	–	−39.27	–	−35.5	–
Fractional bandwidth (%)	18.11	18.14	18.18	18.52	25.40	25.87

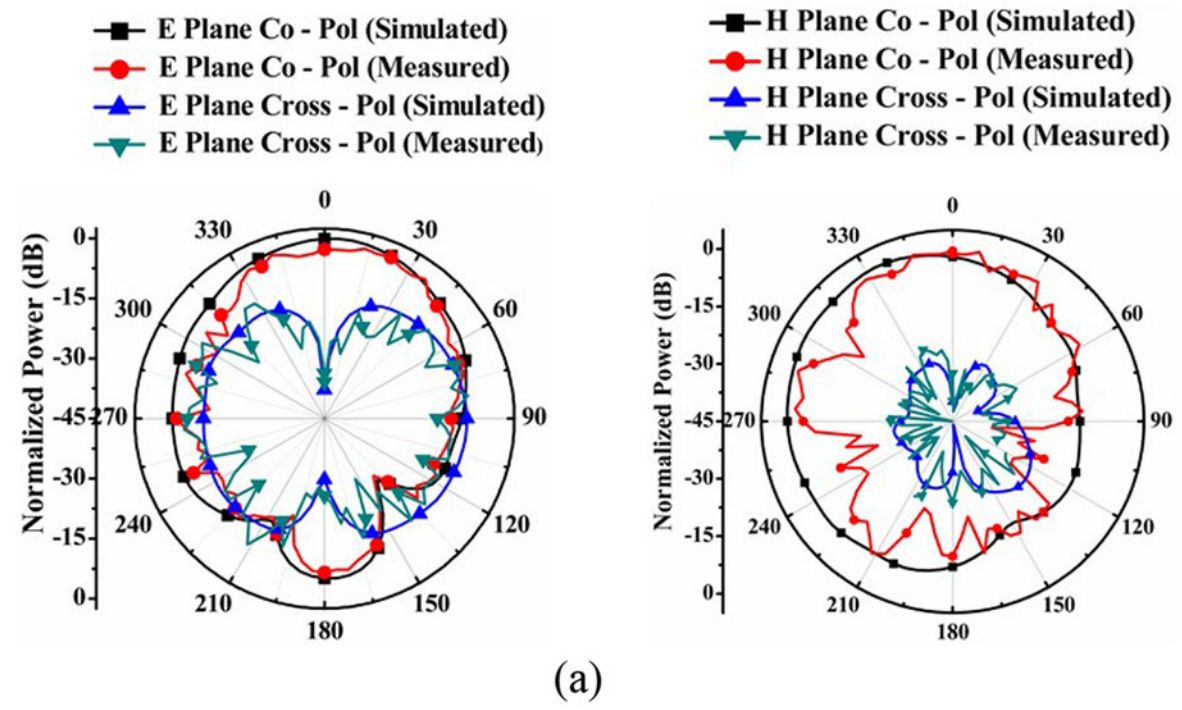

(a)

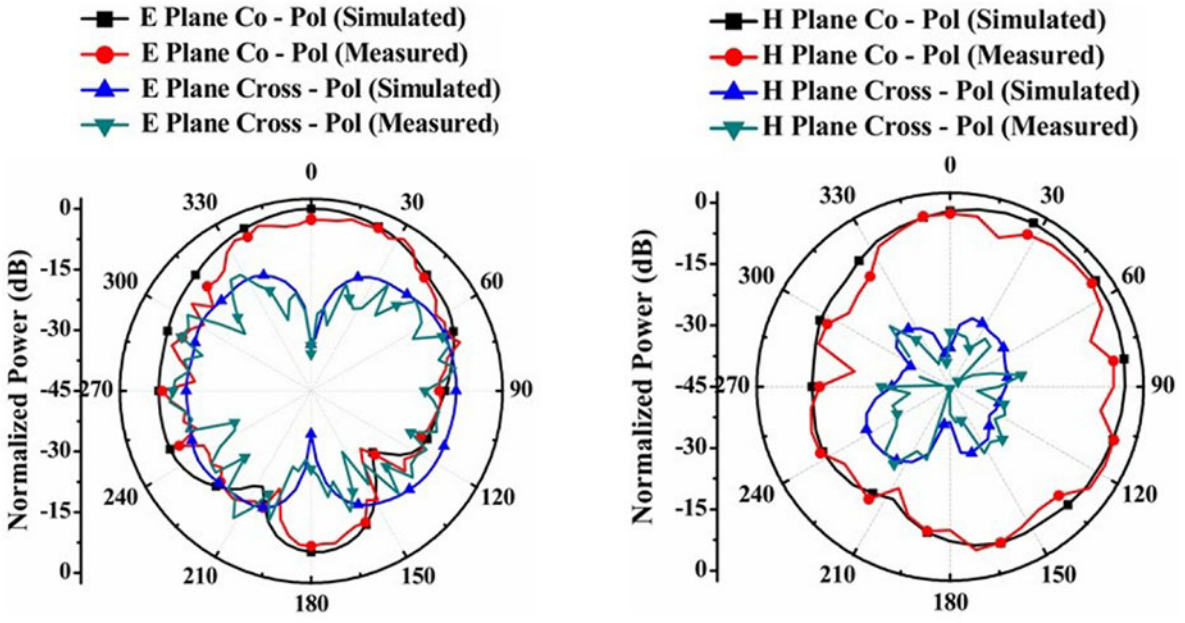

(b)

Figure 18. Comparison between simulated and measured radiation pattern: (a) Port-1 at 5.58 GHz and (b) Port-2 at 5.6 GHz.

https://doi.org/10.1017/S1759078724000862 Published online by Cambridge University Press

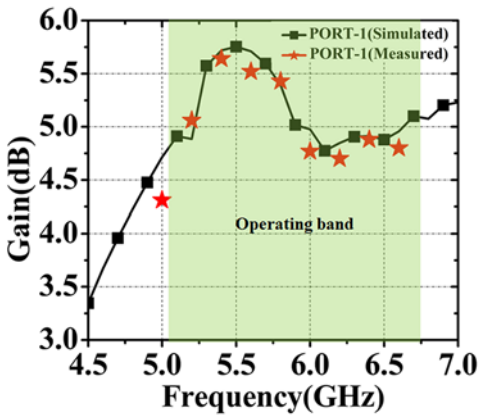

Figure 19. Comparison between simulated and measured Gain.

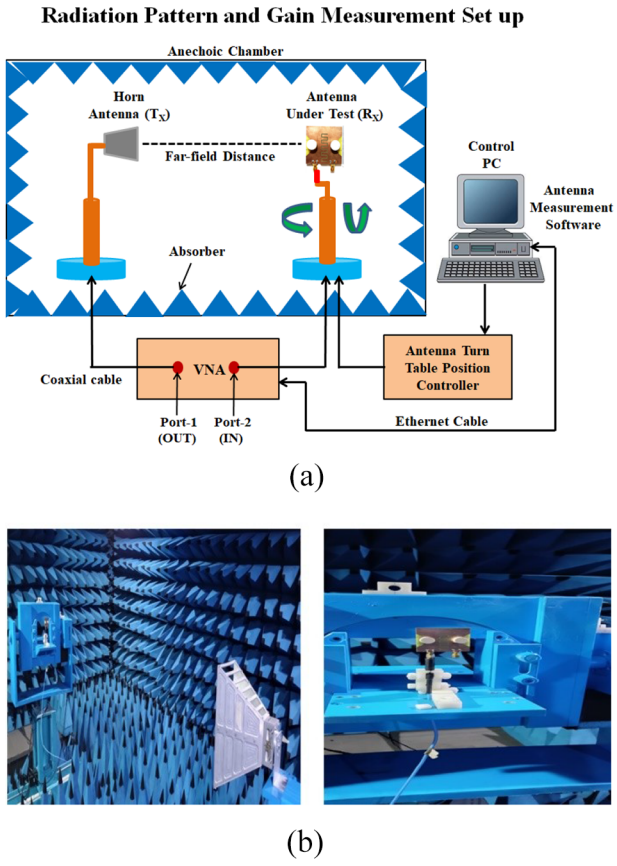

Figure 20. Far-field measurement setup (for radiation pattern and gain): (a) Block diagram (b) Anechoic chamber.

The block diagram to measure the far-field gain and radiation patterns is illustrated in Fig. 20(a). The gain measurement of the proposed antenna utilizes the gain-comparison method, requiring a reference antenna with a known gain and a horn antenna whose gain is not known. These measurements are managed by software on a PC, with the computer transmitting synchronization pulses via Ethernet to the VNA at the start of each procedure. The antennas must be coaxially aligned. The positioner aligns the antennas by adjusting the antenna under test's (AUT's) height, azimuth, and elevation for maximum received power, computed using the Friis transmission equation [39]. For far-field radiation pattern measurement, the horn antenna and AUT are placed in the chamber for line-of-sight communication, with absorbers mitigating reflected EM radiation. The AUT rotates through azimuth, elevation, and polarization axes using a position controller.The horn antenna is energized by a VNA, causing it to radiate, while the AUT receives these signals in S_{21} mode, interfaced with the VNA which extracts the results and feeds them to PC software to plot the far-field patterns. Measurement precision is affected by system interconnections and RF cable movement, while accuracy depends on motor movements, probe influence, and RF connectors. All measuring instruments are calibrated before antenna measurement to minimize errors. Figure 20(b) shows the physical arrangement within an automatic anechoic chamber for experimental assessment of radiation patterns and gain.

Diversity parameters of MIMO antenna

ECC, DG, MEG, TARC, and CCL are the metrics to determine the diversity performance of the proposed two-port radiator [3]. The level of field correlation among the various antenna elements in the MIMO radiator is determined by the ECC performance parameter, which is a crucial diversity performance parameter. It illustrates how the radiation patterns of the individual radiator elements would affect each other when all the ports are operated concurrently. ECC can be estimated using scattering parameters and far-field patterns. The MIMO antenna having higher radiation efficiency (~90%) is estimated using scattering parameters, and those having lower radiation efficiency are calculated using the far-field method. Equations (4) and (5) present an estimation of ECC for a dual port MIMO radiator using scattering parameters and the far-field method [40]. The proposed two-port radiator attains high radiation efficiency (>93%) within the band of interest, so equation (4) can be utilized to calculate ECC for the proposed two-port radiator. ECC should be less than 0.5 in any MIMO radiator.

$$ECC = |\varrho_{12}|^2 \left| \frac{|S_{12}{}^{*}S_{12} + S_{21}{}^{*}S_{22}|}{|(1 - |S_{11}|^2 - |S_{21}|^2)\left(1 - |S_{22}|^2 - |S_{12}|^2\right)|^{1/2}} \right|^2 \tag{4}$$

$$ECC_F = \frac{\left| \iint_{4\pi} \left[A_i(\theta,\varphi)^{*} A_j(\theta,\varphi)\, d\omega \right] \right|^2}{\iint_{4\pi} |A_i(\theta,\varphi)|^2 \iint_{4\pi} |A_j(\theta,\varphi)|^2 d\omega} \tag{5}$$

Figure 21 represents the comparative analysis of the simulated and experimentally observed ECC for the proposed two-port radiator. The simulated and experimentally observed ECC are found within optimal limits. DG, a crucial parameter, refers to the enhancement in signal-to-noise ratio observed in multiple antenna systems when compared to single antenna systems. For the MIMO antenna design, a high DG value is imperative, nearly 10 dB in the operational bandwidth, to ensure good reliability and performance [3]. Equation (6) is adapted to estimate the DG of the proposed two-port radiator [3].

$$DG = 10\sqrt{1 - ECC^2} \tag{6}$$

A comparison between the simulated and measured DG is depicted in Fig. 22, and it can be seen that the simulated and measured DGs are similar to each other within the band of operation. MEG serves as another significant diversity parameter.

https://doi.org/10.1017/S1759078724000862 Published online by Cambridge University Press

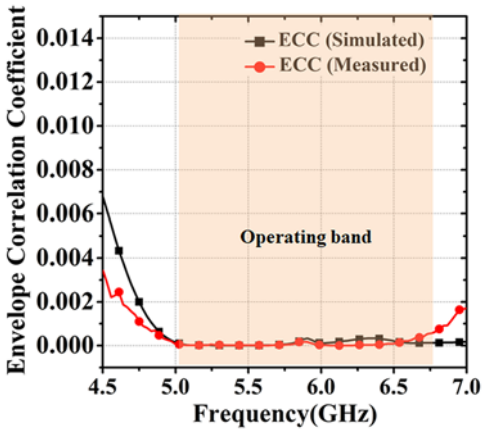

Figure 21. Comparison between simulated and measured ECC.

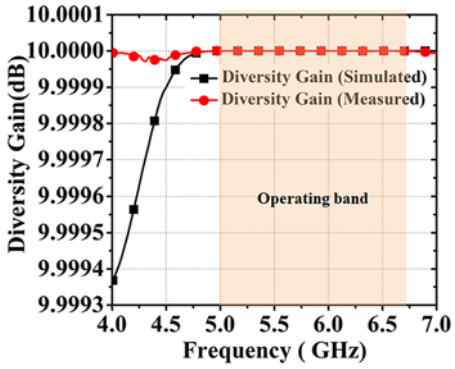

Figure 22. Comparison between simulated and measured DG.

It is a metric utilized to compare the power captured by a diversity radiator in a fading environment with the power received by an isotropic radiator. Suppose the statistical environment is homogeneous with equal vertical and horizontal polarization power densities. MEG corresponds to half of the radiation efficiencies [23]. For the *i*th port MIMO antenna, MEG is estimated using equation (7) as reported in Ref. [23].

$$\mathrm{MEG_i} = 0.5\left[1 - \sum_{j=1}^{N} |S_{ij}|^2\right] \tag{7}$$

MEG-1 and MEG-2 are the mean effective gain of the two-port MIMO antenna. The ratio of MEG-1 to MEG-2 (MEG-1/MEG2) for a decent MIMO antenna system with the same power level should be $\leq$3 dB. For better performance, the difference should be between 0 and −3 dB [3, 23]. A comparison between simulated and measured MEG is reported in Fig. 23. It is observed that the measured MEG is close to the simulated MEG within the band of operation. Another important diversity parameter is the CCL. CCL is of significant importance as a diversity performance metric, signifying the maximum achievable message transmission rate for delivering a signal repeatedly through a communications system. The following formula (equation 8) can be used to compute it [41]:

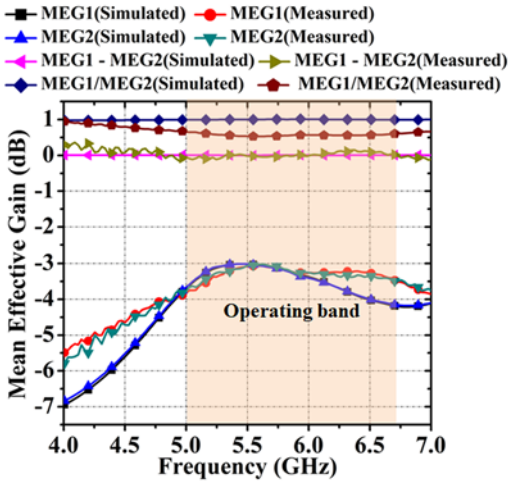

Figure 23. Comparison between simulated and measured MEG.

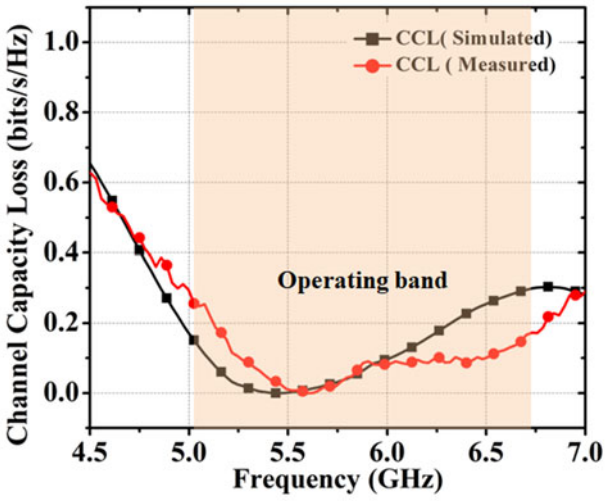

Figure 24. Comparison between simulated and measured CCL.

$$\begin{aligned} \mathrm{CCL} &= -\log_2 \det \begin{pmatrix} \beta_{11} & \beta_{12} \\ \beta_{21} & \beta_{22} \end{pmatrix} \\ \beta_{11} &= \left(1 - \left(|S_{11}|^2 + |S_{12}|^2\right)\right) \\ \beta_{22} &= \left(1 - \left(|S_{22}|^2 + |S_{21}|^2\right)\right) \\ \beta_{21} &= -\left(S^*_{22}S_{21} + S^*_{12}S_{21}\right) \end{aligned} \tag{8}$$

The highest permissible limit for CCL is 0.4 bits/s/Hz for any MIMO antenna structure. A comparison between simulated and experimentally observed CCL curves has been presented in Fig. 24. It is found that both simulated and measured values of CCL are within optimal limits. However, some variations exist among simulated and experimentally observed values because of fabrication and measurement tolerances, as discussed in the "Experimental results" section. Another crucial MIMO performance metric for accurately describing the MIMO radiator is TARC. TARC is a technique for a two-port radiator that compresses all the data from the S-parameters into a single curve. The two-port MIMO antenna system's resonant frequency and impedance bandwidth are thus

https://doi.org/10.1017/S1759078724000862 Published online by Cambridge University Press

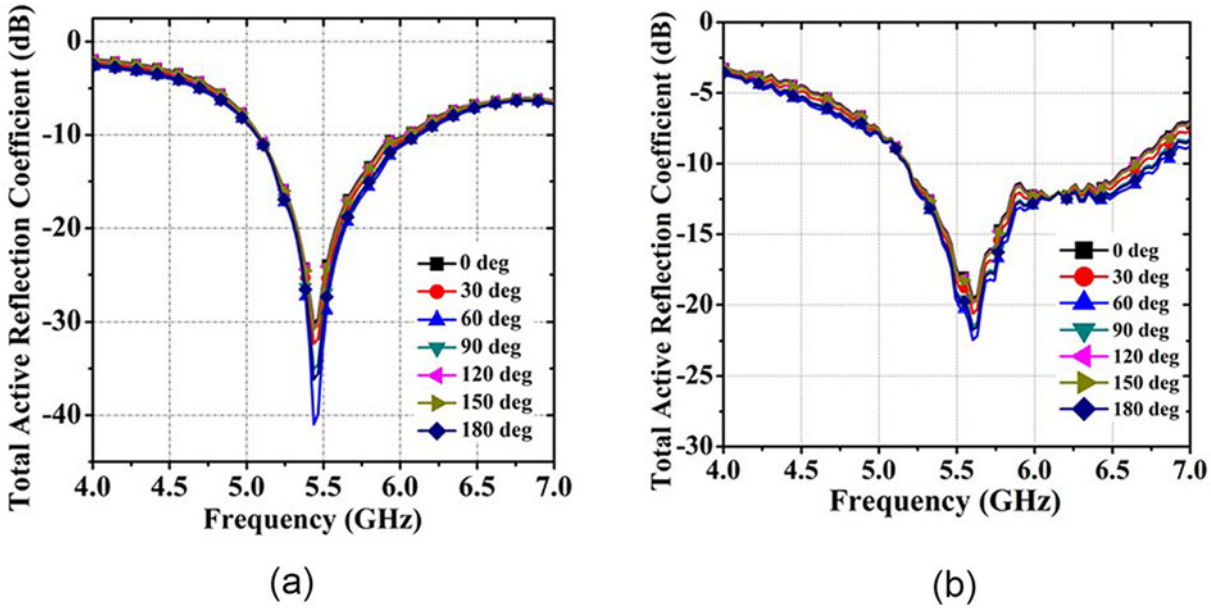

Figure 25. Comparison between simulated and measured TARC: (a) Simulated (b) Measured.

Table 4. Comparative analysis between proposed work and existing work available in the literature

Ref. no	Antenna dimension (mm^3)	Isolation technique	Isolation (dB) at resonant frequency	Frequency range (GHz)	% Bandwidth (fractional)	ECC	DG(dB)	Fabrication complexity
[23]	90 × 90 × 25.6	Excitation of orthogonal modes	−18	1.69–1.96	7.3	<0.02	9.9	Complex
[24]	50 × 50 × 9.6	Excitation of orthogonal modes	−32	4.9–5.5	11.5	–	–	Easy
[25]	50 × 50 × 14.6	Excitation of orthogonal modes	−25	3.1–3.68 (Port-1)	17.818.4	–	–	Easy
				3.1–3.70 (Port-2)				
[26]	20 × 20 × 2.794	Metal strip printed on DRA	−24	27.5–28.35	3	0.013	9.9	Complex
[27]	120 × 70 × 9.67	Metal strip printed on DRA	−28	4.73–5.1	7.52	<0.05	>9.8	Complex
[28]	120 × 70 × 9.67	Orthogonal feeding	−22.5	4.48–4.60	2.64	0.037	9.99	Moderate
				4.98–5.04	1.2			
[29]	60 × 60 × 5.787	Use of split-ring resonator loaded on a vertical substrate	−30	7.4–7.8	5.26	–	–	Complex
Proposed work	**50 × 50 × 8.5**	**Use of interdigital + semi-circular arc-shaped DGS**	**−35.5**	**5.19–6.7 (Port-1) 5.15–6.68 (Port-2)**	**25.4 25.87**	**<0.0004**	**10**	**Easy**

calculated using a single TARC curve. TARC can be calculated using equation (9) for a dual port MIMO radiator [3, 41].

$$TARC(\Gamma_a^t) = \sqrt{\frac{\left(\left(|S_{11} + S_{12e^{j\theta}}|^2\right) + \left(|S_{21} + S_{22e^{j\theta}}|^2\right)\right)}{2}} \quad (9)$$

where S_{12} is the isolation amidst the two ports, S_{11} and S_{22} are the reflection coefficients of Port-1 and Port-2 of the antenna framework, and θ is the phase angle of the input feed.

Figure 25(a) and Fig. 25(b) illustrate the TARC curves for the proposed two-port radiator setup. Figure 25(a) shows the simulated TARC, while Fig. 25(b) presents the measured TARC plot. A variation in the simulated and measured TARC plots is observed. This may be due to the fabrication tolerances of the proposed prototype two-port radiator. The phase angle of the input feed varies between 0° and 180° with an interval of 30° to determine the resonating behavior of the proposed radiator. It can be observed in Fig. 25 that, regardless of the phase angle of the input feed, the effective impedance and resonant peak bandwidth remain constant. A comparative analysis between the proposed work and existing MIMO antennas available in literature in terms of isolation technique, isolation, operating band, ECC, DG, and fabrication complexity has been reported in Table 4.

https://doi.org/10.1017/S1759078724000862 Published online by Cambridge University Press

Conclusion

An aperture coupled offset fed DR-based two-port MIMO antenna, utilizing a combination of arc and interdigital-shaped line DGS for isolation and bandwidth enhancement, has been illustrated in this letter. For the proposed two-port radiator, the frequency band of interest is determined to be 5.19–6.7 and 5.15–6.68 GHz for Port-1 and Port-2, respectively. The isolation between the radiators is obtained to be −35.5 dB. It demonstrates remarkable ECC and DG within the operational band. Other MIMO diversity parameters, such as MEG, TARC, and CCL, have been computed and determined to be within permissible limits. The simulated and measured results exhibit a high degree of agreement, showing only slight deviations. The antenna is helpful for WLAN and WiMAX applications.

Acknowledgments. The authors express their gratitude to Dr. Ravi Kumar Gangwar, Professor in the Department of Electronics and Communication Engineering, for his valuable cooperation in conducting antenna measurements (DST-FIST supported) at the Indian Institute of Technology (Indian School of Mines), Dhanbad, India.

Competing interests. The researchers confirm the absence of any identifiable financial or personal conflicts that could have seemed to influence the findings presented in this study.

References

1. **Zhou Q and Dai H** (2006) Joint antenna selection and link adaptation for MIMO systems. *IEEE Transactions on Vehicular Technology* **55**(1), 243–255
2. **Keyrouz S and Caratelli D** (2016) Dielectric resonator antennas: basic concepts, design guidelines, and recent developments at millimeter-wave frequencies. *International Journal of Antennas and Propagation* **2016**, 1–20.
3. **Sharawi MS** (2014) *Printed MIMO Antenna Engineering*. Boston, MA: Artech House.
4. **Anuar SU, Jamaluddin MH, Din J, Kamardin K, Dahri MH and Idris IH** (2020) Triple band MIMO dielectric resonator antenna for LTE applications. *AEU - International Journal of Electronics and Communications* **118**, 153172.
5. **Sharawi MS** (2013) Printed multi-band MIMO antenna systems and their performance metrics [wireless corner]. *IEEE Antennas and Propagation Magazine* **55**(5), 218–232.
6. **Margaret DH, Subasree MR, Susithra S, Keerthika SS and Manimegalai B**, "Mutual coupling reduction in MIMO antenna system using EBG structures," *2012 Int. Conf. Signal Process. Commun. SPCOM 2012*, 2012.
7. **Tadesse AD, Acharya OP and Sahu S** (2023) Wideband MIMO antenna mutual coupling reduction with electromagnetic band-gap structure. *IETE Journal of Research* **69**(9), 6014–6021.
8. **Kumar A and De A** (2023) Novel H-shaped EBG in E-plane for isolation enhancement of compact CPW-fed two-port UWB MIMO antenna. *IETE Journal of Research* **69**(9), 5986–5992.
9. **Zhang S and Pedersen GF** (2016) Mutual coupling reduction for UWB MIMI antennas with a wideband neutralization line. *IEEE Antennas and Wireless Propagation Letters* **15**, 166–169.
10. **Li Z, Saito K, Saito K and Ito K** (2012) Reducing mutual coupling of MIMO antennas with parasitic elements for mobile terminals. *IEEE Transactions on Antennas and Propagation* **60**(2 PART 1), 473–481
11. **Tran HH and Nguyen-Trong N** (2021) Performance enhancement of MIMO patch antenna using parasitic elements. *IEEE Access* **9**, 30011–30016.
12. **Sim CYD, Dhasarathan V, Tran TK, Kulkarni J, Garner BA and Li Y** (2023) Mutual coupling reduction in dual-band MIMO antenna using parasitic dollar-shaped structure for modern wireless communication. *IEEE Access* **11**(January), 5617–5628.
13. **Farahani M, Pourahmadazar J, Akbari M, Nedil M, Sebak AR and Denidni TA** (2017) Mutual coupling reduction in millimeter-wave MIMO antenna array using a metamaterial polarization-rotator wall. *IEEE Antennas and Wireless Propagation Letters* **16**, 2324–2327.
14. **Dwivedi AK, Sharma A, Singh AK and Singh V** (2021) Metamaterial inspired dielectric resonator MIMO antenna for isolation enhancement and linear to circular polarization of waves. *Measurement* **182**(May), 109681.
15. **Madni A, Hasan Bilal RM and Khan WT** (2022) A compact metamaterial based high isolation MIMO antenna for 5.8 GHz WLAN applications. *2022 IEEE International Symposium on Antennas and Propagation and USNC-URSI Radio Science Meeting (AP-S/URSI 2022)* (1), 245–246.
16. **Ali Esmail B and Koziel S** (2023) High isolation metamaterial-based dual-band MIMO antenna for 5G millimeter-wave applications. *AEU - International Journal of Electronics and Communications* **158**, 154470.
17. **Dadgarpour A, Zarghooni B, Denidni TA and Kishk AA** (2017) Mutual coupling reduction in dielectric resonator antennas using metasurface shield for 60-GHz MIMO systems. *IEEE Antennas and Wireless Propagation Letters* **16**, 477–480.
18. **Dubazane SP, Kumar P and Afullo TJO** (2022) Metasurface superstrate-based MIMO patch antennas with reduced mutual coupling for 5G communications. *Applied Computational Electromagnetics Society Journal* **37**(4), 408–419.
19. **Karimian R, Kesavan A, Nedil M and Denidni TA** (2017) Low-mutual-coupling 60-GHz MIMO antenna system with frequency selective surface wall. *IEEE Antennas and Wireless Propagation Letters* **16**, 373–376.
20. **Sarkar GA, Ballav S, Chatterje A, Ranjit S and Parui SK** (2019) Four element MIMO DRA with high isolation for WLAN applications. *Progress In Electromagnetics Research Letters* **84**(May), 99–106.
21. **Ibrahim AA, Abdalla MA, Abdel-Rahman AB and Hamed HFA** (2014) Compact MIMO antenna with optimized mutual coupling reduction using DGS. *International Journal of Microwave and Wireless Technologies* **6**(2), 173–180.
22. **Divya G, Jagadeesh Babu K and Madhu R** (2021) Quad-band hybrid DRA loaded MIMO antenna with DGS for isolation enhancement. *International Journal of Microwave and Wireless Technologies* **14**(2), 1–10.
23. **Nasir J, Jamaluddin MH, Khalily M, Kamarudin MR, Ullah I and Selvaraju R** (2015) A reduced size dual port MIMO DRA with high isolation for 4G applications. *International Journal of RF and Microwave Computer-Aided Engineering* **25**(6), 495–501.
24. **Das G, Sharma A and Gangwar RK** (2017) Dual feed MIMO cylindrical dielectric resonator antenna with high isolation. *Microwave and Optical Technology Letters* **59**(7), 1686–1692.
25. **Das G, Sharma A and Gangwar RK** (2017) Dual port aperture coupled MIMO cylindrical dielectric resonator antenna with high isolation for WiMAX application. *International Journal of RF and Microwave Computer-Aided Engineering* **27**(7), 1–10.
26. **Zhang Y, Deng J-Y, Li M-J, Sun D and Guo L-X** (2019) A MIMO dielectric resonator antenna with improved isolation for 5G mm-wave applications. *IEEE Antennas and Wireless Propagation Letters* **18**(4), 747–751.
27. **Elahi M, Altaf A, Almajali E and Yousaf J** (2022) Mutual coupling reduction in closely spaced MIMO dielectric resonator antenna in H-plane using closed metallic loop. *IEEE Access* **10**, 71576–71583.
28. **Upadhyaya T, Park I, Pandey R, Patel U, Pandya K, Desai A, Pabari J, Byun G and Kosta Y** (2022) Aperture-fed quad-port dual-band dielectric resonator-MIMO antenna for sub-6 GHz 5G and WLAN application. *International Journal of Antennas and Propagation* **2022**, 1–13.
29. **Mishra NK, Acharjee J, Sharma V, Tamrakar C and Dewangan L** (2022) Mutual coupling reduction between the cylindrical dielectric resonator antenna using split ring resonator based structure. *AEU - International Journal of Electronics and Communications* **154**(June), 154305.
30. **Kang L, Li H, Wang X and Shi X** (2015) Compact offset microstrip-Fed MIMO antenna for band-notched UWB applications. *IEEE Antennas and Wireless Propagation Letters* **14**, 1754–1757.
31. **Chung KL and Kharkovsky S** (2013) Mutual coupling reduction and gain enhancement using angular offset elements in circularly polarized patch array. *IEEE Antennas and Wireless Propagation Letters* **12**, 1122–1124.
32. **Arya AK, Kartikeyan MV and Patnaik A** (2010) Defected ground structure in the perspective of microstrip antennas: A review. *Frequenz* **64**(5–6), 79–84.

https://doi.org/10.1017/S1759078724000862 Published online by Cambridge University Press

33. **Khandelwal MK, Kanaujia BK and Kumar S** (2017) Defected ground structure: Fundamentals, analysis, and applications in modern wireless trends. *International Journal of Antennas and Propagation* **2017**, 1–22.
34. **Balalem A, Ali AR, Machac J and Omar A** (2007) Quasi-elliptic microstrip low-pass filters using an interdigital DGS slot. *IEEE Microwave and Wireless Components Letters* **17**(8), 586–588
35. **Mongia RK and Bhartia P** (1994) Dielectric resonator antennas – A review and general design relations for resonant frequency and bandwidth. *International Journal of Microwave and Millimeter-Wave Computer Aided Engineering* **4**(3), 230–247
36. **Petosa A** (2007) *Dielectric Resonator Antenna Handbook*. Boston, MA: Artech House.
37. **Khaleel SA, Hamad EKI, Parchin NO and Saleh MB** (2022) MTM-inspired graphene-based THz MIMO antenna configurations using characteristic mode analysis for 6G/IoT applications. *Electron* **11**(14), 2152
38. **Aras MSM, Rahim MKA, Asrokin A and Abdul Aziz MZA**, "Dielectric resonator antenna (DRA) for wireless application," 2008 IEEE International RF and Microwave Conference, Kuala Lumpur, Malaysia, 2008, 454–458.
39. **Balanis CA** (2016) *Antenna Theory: Analysis and Design*. Hoboken, NJ: John wiley & sons.
40. **Blanch Ss, Romeu J and Corbella I** (2003) Exact representation of antenna system diversity performance from input parameter description. *Electronics Letters* **39**(9), 705–707
41. **Chae SH, Oh SK and Park SO** (2007) Analysis of mutual coupling, correlations, and TARC in WiBro MIMO array antenna. *IEEE Antennas and Wireless Propagation Letters* **6**(6), 122–125

Gouri Shankar Sharma received his B.E degree in Electronics and Communication Engineering from Guru Ghasidas University (Central), Bilaspur (C.G), India, in 2006 and his M.Tech in ECE from the Indian Institute of Technology (Indian School of Mines), Dhanbad, India, in 2013. He is currently Pursuing Ph.D. as a Senior Research Fellow in the Department of Electronics and Communication Engineering, NIT Raipur, India. His research area includes dielectric resonator antenna and MIMO antenna.

Anshul Gupta received his Master of Technology in Microwave Engineering from IIT (Banaras Hindu University) Varanasi, and a Ph.D. in Electronics Engineering from Indian Institute of Technology (Indian School of Mines), Dhanbad, India, in 2011 and 2019, respectively. He has authored or co-authored many research papers in international journals/conference proceedings. He is an assistant professor at the Department of Electronics and Communication Engineering, National Institute of Technology Raipur, Chhattisgarh, India. His research interests include dielectric resonator antennas, 5G MIMO antennas, wideband and multiband antennas, circularly polarized DRAs, and antennas for IoT applications.

https://doi.org/10.1017/S1759078724000862 Published online by Cambridge University Press